

# JGR Space Physics

## RESEARCH ARTICLE

10.1029/2019JA026965

### Key Points:

- A statistical study of EMIC waves is performed using long-term Van Allen Probes data in the inner magnetosphere
- We have presented the distributions of occurrence rate, wave normal angle, and ellipticity for  $H^+$ ,  $He^+$ , and  $O^+$  band waves
- The dependences of the occurrence rate and magnetic amplitude on the  $AE^+$  index are also studied

### Correspondence to:

X. Gao,  
gaoxl@mail.ustc.edu.cn

### Citation:

Chen, H., Gao, X., Lu, Q., & Wang, S. (2019). Analyzing EMIC waves in the inner magnetosphere using long-term Van Allen Probes observations. *Journal of Geophysical Research: Space Physics*, 124, 7402–7412. <https://doi.org/10.1029/2019JA026965>

Received 22 MAY 2019

Accepted 8 AUG 2019

Accepted article online 23 AUG 2019

Published online 3 SEP 2019

## Analyzing EMIC Waves in the Inner Magnetosphere Using Long-Term Van Allen Probes Observations

Huayue Chen<sup>1</sup> , Xinliang Gao<sup>1</sup> , Quanming Lu<sup>1</sup> , and Shui Wang<sup>1</sup>

<sup>1</sup>CAS Key Laboratory of Geoscience Environment, School of Earth and Space Sciences, University of Science and Technology of China, Hefei, China

**Abstract** With 64-month magnetic data from Van Allen Probes, we have studied not only the global distribution, wave normal angle ( $\theta$ ), and ellipticity ( $\epsilon$ ) of electromagnetic ion cyclotron (EMIC) waves, but also the dependence of their occurrence rates and magnetic amplitudes on the  $AE^+$  index (the mean value of  $AE$  index over previous 1 hr). Our results show that  $H^+$  band waves are preferentially detected at  $5 \leq L \leq 6.5$ , in the noon sector. They typically have small  $\theta$  ( $< 30^\circ$ ) and weakly left-hand polarization but become more oblique and linearly polarized at larger magnetic latitudes or L-shells. With the increase of  $AE^+$  index, their occurrence rate significantly increases in the noon sector, and their source region extends to dusk sector.  $He^+$  band waves usually occur in the predawn and morning sectors at  $3 \leq L \leq 4.5$ . They generally have moderate  $\theta$  ( $30^\circ - 40^\circ$ ) and left-hand polarization and also become more oblique and linearly polarized at larger latitudes or L-shells. There is a clear enhancement of occurrence rate and amplitude during active geomagnetic periods, especially in the dusk and evening sectors.  $O^+$  band waves mainly occur at  $3 \leq L \leq 4$  in the predawn sector. They have either very small  $\theta$  ( $< 20^\circ$ ) or very large  $\theta$  ( $> 50^\circ$ ), and typically linear or weakly right-hand polarization. During active periods, they mostly occur at the midnight sector and  $L < 3.5$ . As a valuable supplement to previous statistical studies, our result provides not only a more comprehensive EMIC wave model for evaluating their effects on the radiation belt, but also detailed observational constraints on generation mechanisms of EMIC waves.

## 1. Introduction

Electromagnetic ion cyclotron (EMIC) wave is one of common emissions in the Earth's magnetosphere, whose frequency falls within the range of Pc1–Pc2 (0.1–5 Hz) geomagnetic pulsations (Anderson et al., 1990; Cornwall, 1965; Young et al., 1981). EMIC wave has been considered as an important candidate for heating heavy ions in the inner magnetosphere (Chen et al., 2018; Gao et al., 2013; Thorne & Horne, 1994; Zhang et al., 2011), scattering ring current protons (Carson et al., 2013; Xiao et al., 2011), and the loss of relativistic electrons in the radiation belt (Gao et al., 2015; Meredith et al., 2003; Ni et al., 2015; Zhang et al., 2016). The thermal anisotropy ( $T_\perp > T_\parallel$ ) of hot protons provides the free energy to excite EMIC waves (Anderson et al., 1991; Chen et al., 2011; Cornwall, 1965; Gary et al., 2012; Lu et al., 2006; Lu & Wang, 2006). Since there are different ion species (such as  $H^+$ ,  $He^+$ , and  $O^+$ ) in the magnetosphere, EMIC waves can be divided into three bands (Andre, 1985; Hu et al., 2010):  $H^+$  band between the local  $H^+$  gyrofrequency and  $He^+$  gyrofrequency;  $He^+$  band between the local  $He^+$  gyrofrequency and  $O^+$  gyrofrequency; and  $O^+$  band below the local  $O^+$  gyrofrequency. Both the linear theory (Chen et al., 2009; Horne & Thorne, 1993) and observations (Anderson et al., 1992; Usanova et al., 2013) indicate the main source region of EMIC waves is near the magnetic equator, where is the local minimum of magnetic field strength along one field line, while there also exists the off-equator source region at high L-shells on the dayside, where multiple magnetic field minima are formed due to the compression by solar winds (Anderson & Hamilton, 1993; Usanova et al., 2008).

Previous theoretical (Andre, 1985; Gary et al., 2012) and simulation (Denton et al., 2014; Hu et al., 2010) studies predicted that EMIC waves are generated as transverse, left-handed polarized emissions via proton anisotropy instabilities near the magnetic equator, and then become more linearly polarized and oblique during their propagation toward higher-latitude regions. However, there are also linearly polarized EMIC waves detected within the source region, and their wave normal angles sometimes can be very small (Chen et al., 2018; Yu et al., 2018; Yuan et al., 2018). Besides the propagating effect, some other possible theories have been proposed to explain the generation of such linearly polarized EMIC wave. In a multi-ion

plasma, there could be a polarization reversal (from left-hand to linear) in the vicinity of crossover frequency for EMIC waves (Sakaguchi et al., 2013). Besides, the linearly polarized EMIC wave can be driven by protons with a loss-cone distribution (Denton et al., 1992) or caused by the superposition of more than one wave modes (Denton et al., 1996). However, there are still lack of direct observation evidences. As a result, the generation mechanisms of various EMIC waves are still under debate.

A comprehensive statistical analysis of EMIC waves is important for understanding their generation mechanism and modeling their effects on the radiation belt. CRRES observations suggest that both  $H^+$  band and  $He^+$  band EMIC waves are most prevalent in the dusk sector (Meredith et al., 2014). Although CRRES satellite was orbiting at the ideal equatorial region, that is, the main source region of EMIC waves, the MLT coverage is nonuniform and limited due to its short lifetime. Due to the polar orbit of Cluster satellites, Allen et al. (2015) presented the dependence of occurrence and properties of EMIC waves (ignoring different bands) on the magnetic latitude with Cluster observations. Time History of Events and Macroscale Interactions during Substorm (THEMIS) probes can provide a good coverage over MLT at the equatorial region but at relatively larger L-shells, which indicate  $H^+$  band waves preferentially occur in the early morning, while  $He^+$  band waves often occur in the afternoon (Min et al., 2012). As a complement to THEMIS mission, Van Allen Probes, orbiting near the magnetic equator, can cover all MLT in the inner magnetosphere. Using the first 22-month data from Van Allen Probes, Saikin et al. (2015) have found that  $H^+$  band EMIC waves usually occur in prenoon and afternoon sectors, while  $He^+$  band waves feature an overall stronger dayside occurrence. Moreover, they also pointed out the occurrence peak of  $O^+$  band EMIC waves is in the morning sector. Another statistical study of EMIC waves in the inner magnetosphere with Van Allen Probes data was preformed by Jun et al. (2019a, 2019b), which mainly focused on the relationship between EMIC waves and particle injections.

In this study, we have thoroughly investigated  $H^+$  band,  $He^+$  band, and  $O^+$  band EMIC waves by analyzing Van Allen Probes data but over a prolonged time period from September 2012 to December 2017. We have also presented the global distributions of the occurrence rate, wave normal angle, and ellipticity of EMIC waves, but they are quite different from the statistics given by Saikin et al. (2015). Moreover, we have further studied how their occurrence and amplitude depend on the  $AE^*$  index. The organization of this paper is as follows. In section 2 we describe the instruments and analysis methods. The observation results are illustrated in section 3. At last, we summarize the principle results and give some discussions in section 4.

## 2. Instruments and Analysis Methods

The Van Allen Probes, consisting of two identical probes (A and B), is operating in a near-equatorial, highly elliptical, and low-inclination ( $\sim 10^\circ$ ) orbit with perigees of  $1.1R_E$  and apogees of  $5.8R_E$  (Kessel et al., 2012; Mauk et al., 2013). Their precise orbits are slightly different, leading to one spacecraft lapping the other about every 2.5 months (Mauk et al., 2013). These satellites were launched on 30 August 2012, making highly accurate in situ measurements of wave environment and particle fluxes in the plasmasphere, ring current, and radiation belts. The Electric and Magnetic Field Instrument and Integrated Science (EMFISIS) on board both probes can provide high-resolution magnetic field measurements for low-frequency waves (Kletzing et al., 2013). The satellite position information is provided by Science Operations Center in Energetic Particle, Composition, and Thermal Plasma (Spence et al., 2013) Suite, and the corresponding L, magnetic local time (MLT), and magnetic latitude (MLAT) values are estimated by TS04D model (Tsyganenko & Sitnov, 2005).

All the triaxial magnetic field data (64 samples per second) from both probes have been transformed to the mean field aligned coordinate from the  $UVW$  coordinate. Here, the background magnetic field is determined by a 1-s sliding average of magnetic field data. Then, we perform short-time fast Fourier transform (FFT) with the width of FFT window of 64 s (4,096 data points) and the sliding step of 8 s (512 data points) to calculate the power spectra density (PSD) of each magnetic field component. Therefore, the time resolution of PSD is 8 s, and its frequency resolution is 0.0078 Hz. For each band, we will calculate its total power at every time point, and temporarily record those time points with the total power larger than  $0.01 \text{ nT}^2/\text{Hz}$ . To avoid background noises, we further require each EMIC wave event should last for at least 5 min (Saikin et al., 2015). Finally, all time points satisfying above criteria will be collected into

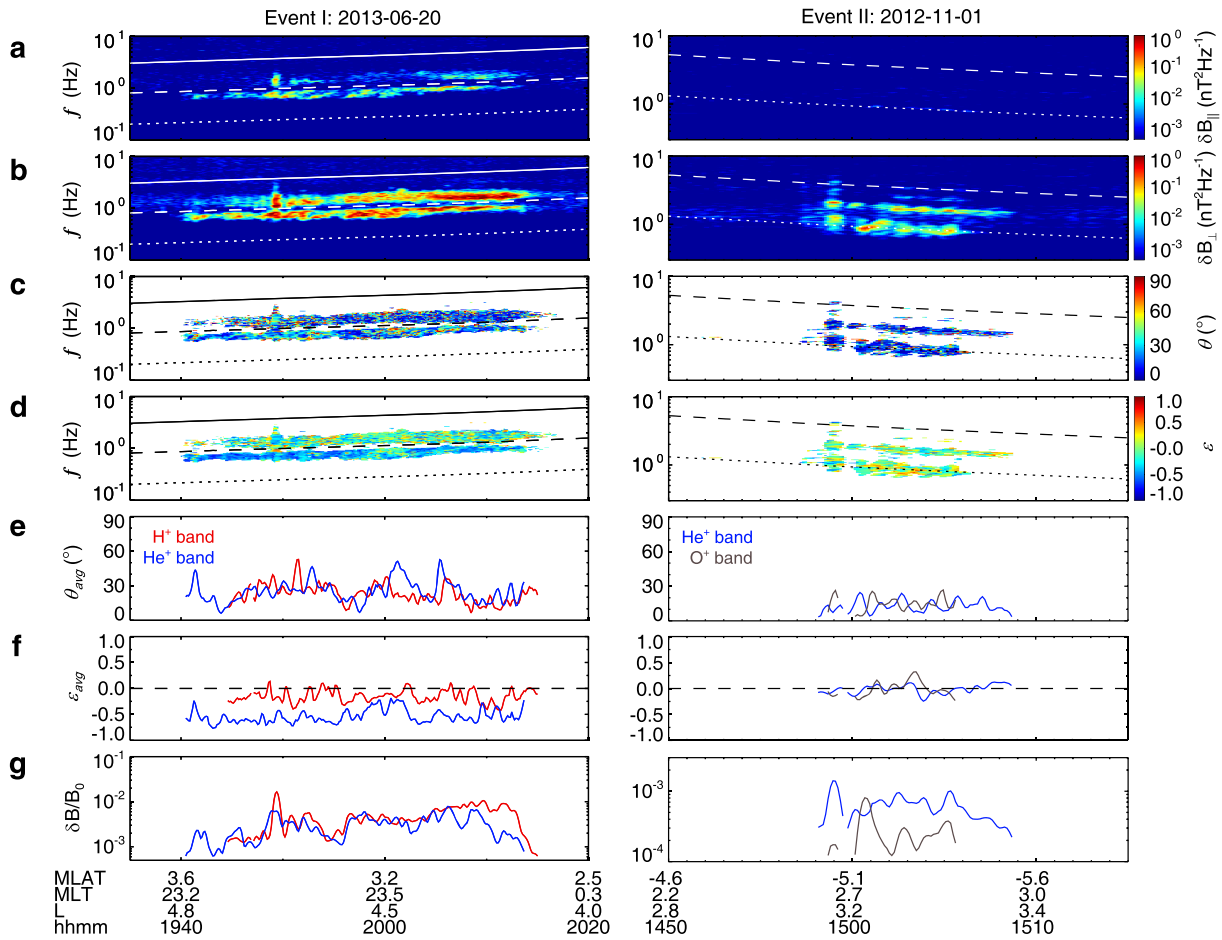


**Figure 1.** The overview of two electromagnetic ion cyclotron wave events observed by Probe B on 20 June 2013 (Event I) and 1 November 2012 (Event II), including (a) parallel and (b) perpendicular magnetic fluctuations, (c) wave normal angle  $\theta$ , (d) ellipticity  $\varepsilon$ , power-weighted average (e) wave normal angle  $\theta_{avg}$  and (f) ellipticity  $\varepsilon_{avg}$  for each band, and (g) magnetic amplitude for each band. The solid, dashed, and dotted lines in white or black in the top four panels denote the local gyrofrequency of proton  $f_{cH^+}$ , helium  $f_{cHe^+}$ , and oxygen  $f_{cO^+}$ , respectively. And the dashed line in Figure 1f corresponds to  $\varepsilon_{avg} = 0$ . MLT = magnetic local time; MLAT = magnetic latitude.

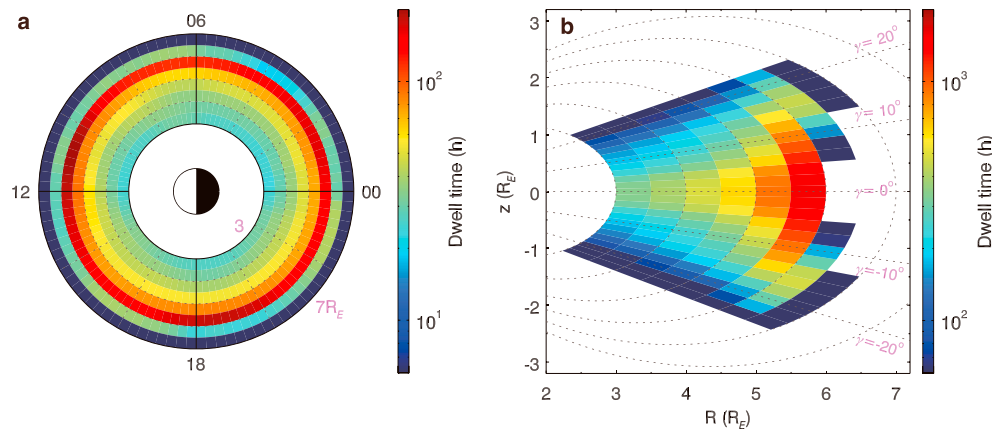


**Figure 2.** The distribution of total dwell time for both probes in the (a) L-MLT and (b) L-MLAT plane at L-shells  $3 \leq L \leq 7$ , during the time period from 8 September 2012 to 31 December 2017. We divide the plane into bins of (a)  $0.5L \times 0.25$  MLT and (b)  $0.5L \times 2$  MLAT, respectively. The dashed curves in Figure 2b denote the dipole field lines  $R = L \cos^2 \gamma$ , where  $\gamma$  represents the magnetic latitude.

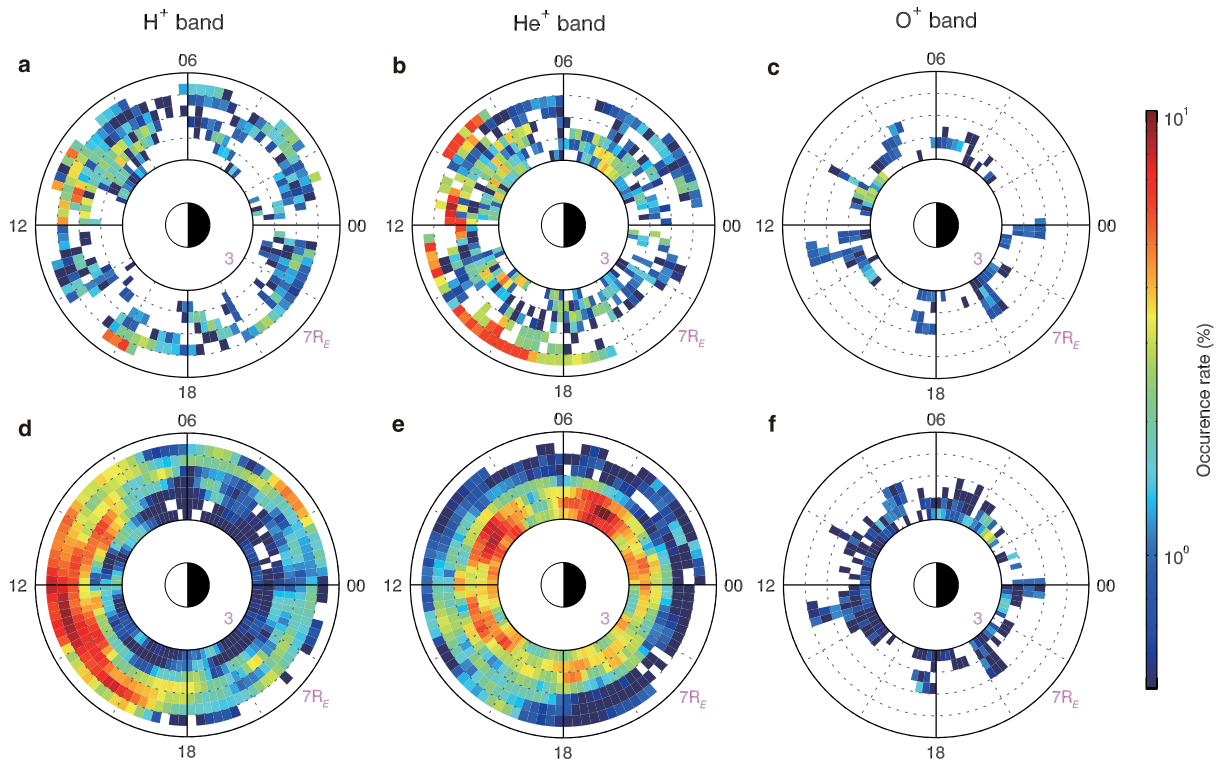


**Figure 3.** The distribution of occurrence rate for all three band waves in L-MLT plane in time ranges of (a–c) 8 September 2012 to 30 June 2014 and (d–f) 8 September 2012 to 31 December 2017. The three columns from left to right correspond to  $H^+$  band,  $He^+$  band, and  $O^+$  band electromagnetic ion cyclotron waves, respectively.

our database for each band. During the period from September 2012 to December 2017, there are 1,379  $H^+$  band wave events (total time of data points is 897.35 hr), 1,193  $He^+$  band wave events (total time is 743.12 hr), and 257  $O^+$  band wave events (total time is 83.27 hr).

### 3. Observational Results

Figure 1 gives two examples of EMIC wave events captured by Probe B, including the spectrogram for (a) parallel and (b) perpendicular magnetic components, (c) wave normal angle  $\theta$ , (d) ellipticity  $\epsilon$ , power-weighted average (e) wave normal angle  $\theta_{avg}$  and (f) ellipticity  $\epsilon_{avg}$  for each band, and (g) magnetic

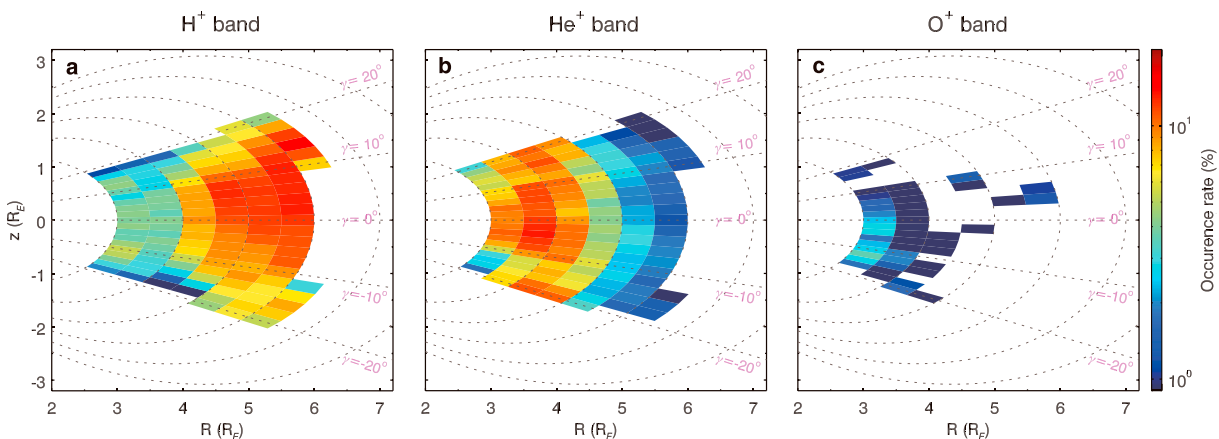


**Figure 4.** The distribution of occurrence rate of  $H^+$  band,  $He^+$  band, and  $O^+$  band waves in the L-MLAT plane.

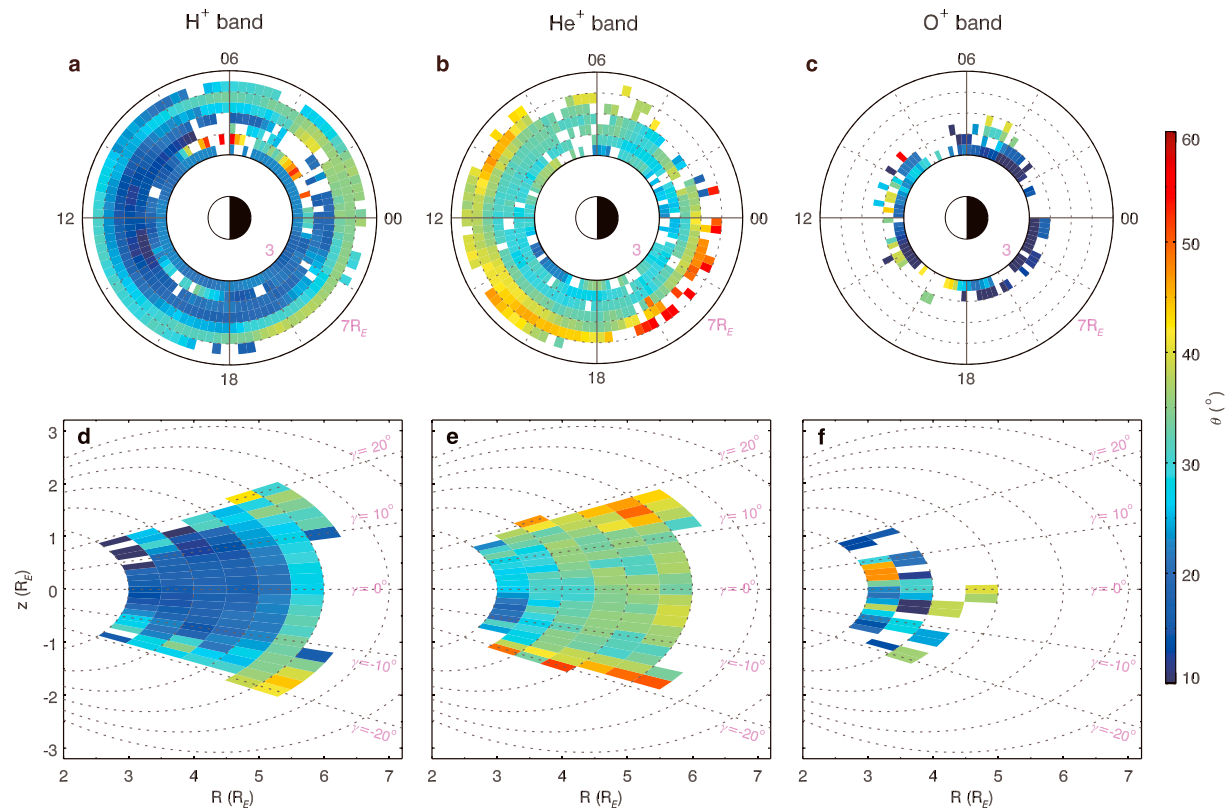


**Figure 5.** The distribution of power-weighted mean wave normal angle of three band waves in the (a–c) L-MLT and (d–f) L-MLAT plane.

amplitude for each band. The solid, dashed, and dotted lines in white or black in Figures 1a–1d denote the local gyrofrequency of proton  $f_{cH^+}$ , helium  $f_{cHe^+}$ , and oxygen  $f_{cO^+}$ , respectively. Here, the wave normal angle and ellipticity are calculated using the algorithm proposed by Means (1972). Note that the negative  $\epsilon$  means left-hand polarization and positive  $\epsilon$  means right-hand polarization. But if the ellipticity is very small ( $\approx 0$ ), then the wave mode is considered to be linearly polarized. Both  $H^+$  band and  $He^+$  band waves are observed in Event I, while both  $He^+$  band and  $O^+$  band waves coexist in Event II. As shown in Figures 1a and 1b, the magnetic power is dominant in the perpendicular direction for each band. All these waves are quasi-parallel propagating to the background magnetic field with wave normal angles smaller than  $30^\circ$  for most of time (Figures 1c and 1e). Remarkably, all wave modes are nearly linearly polarized rather than left-handed polarized except the  $He^+$  band waves in Event I (Figures 1d and 1f), which are quite similar to EMIC waves reported in previous works (Chen et al., 2018).

The distribution of dwell time of available EMFISIS measurements for both probes is displayed in Figure 2 in the (a) L-MLT and (b) L-MLAT planes. The bin size in Figures 2a and 2b is  $0.5L \times 0.25$  MLT and  $0.5L \times 2$  MLAT, respectively. In Figure 2b, the dashed curves represent dipole field lines  $R = L \cos^2 \gamma$ , where  $\gamma$  is the magnetic latitude. We can find that Van Allen Probes provide good coverage between  $L = 3$  and  $6.5$  in all MLT sectors (Figure 2a). Since Van Allen Probes is designed to operate near the equatorial region, the measurements of EMIC waves are mainly limited within  $10^\circ$  of magnetic latitude (Figure 2b).

To compare with the results given by Saikin et al. (2015), Figure 3 shows the occurrence rates of all three band waves ( $H^+$ ,  $He^+$ , and  $O^+$  bands) in the L-MLT plane during two different time periods: 8 September 2012 to 30 June 2014 for the up row and September 2012 to December 2017 for the bottom row. In each bin, the occurrence rate is given by the ratio between the total time of EMIC wave observation and the amount of dwell time that Van Allen Probes have in that bin. In Figures 3a–3c, it is found that  $H^+$  band waves have two maximum occurrence peaks in the prenoon ( $9 \leq \text{MLT} \leq 12$ ) and afternoon ( $15 \leq \text{MLT} \leq 17$ ) sectors, while  $He^+$  band waves have overall stronger probability on the dayside, especially in the outer region  $5.5 \leq L \leq 6.5$ . The



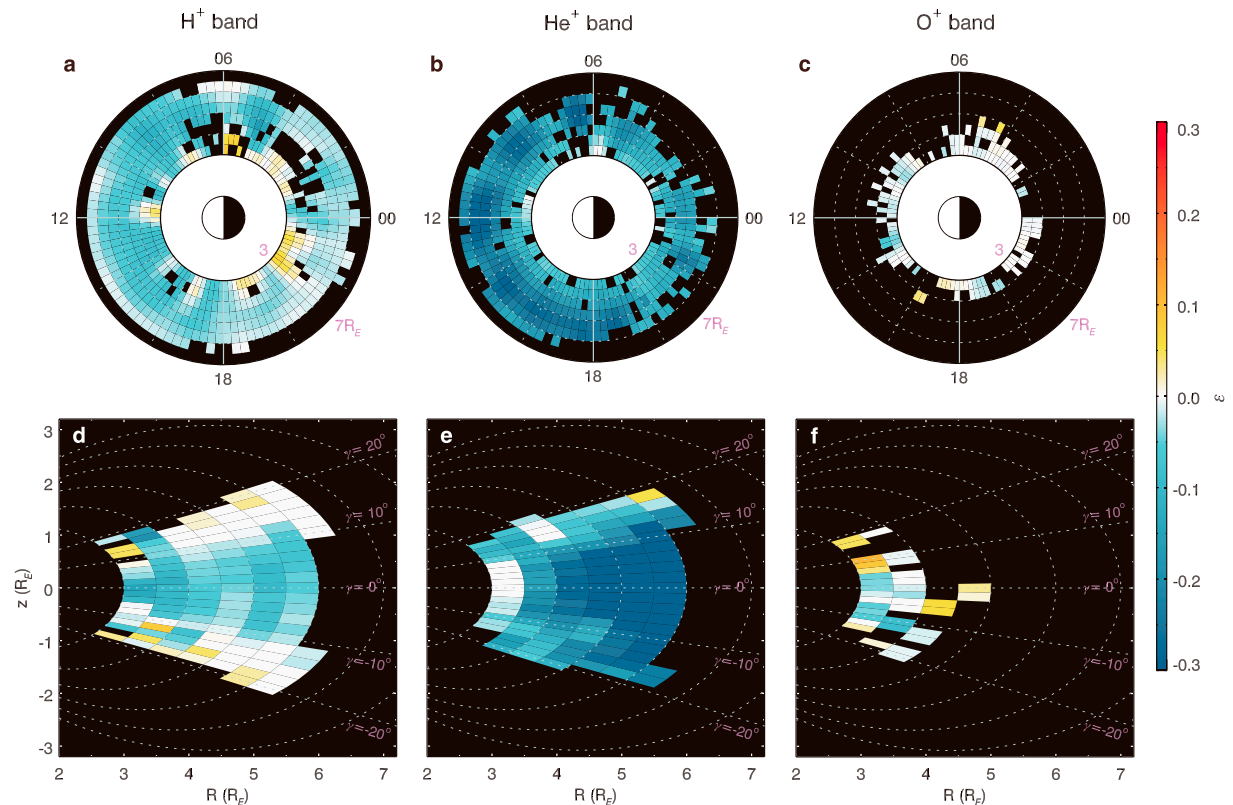


**Figure 6.** The distribution of power-weighted mean ellipticity of three band waves in the (a–c) L-MLT and (d–f) L-MLAT plane.

occurrence rates of O<sup>+</sup> band waves are very low, with a slight increase in the prenoon sector ( $9 \leq \text{MLT} \leq 11$ ) below  $L = 4$ . The above result is just same as that in Saikin et al. (2015). However, in this study, we perform a statistical analysis of EMIC waves over a prolonged time period (about 64 months) and get a different result from the previous study (Saikin et al., 2015). In Figure 3d, we find that H<sup>+</sup> band waves are preferentially detected at relatively larger L-shells ( $5 \leq L \leq 6.5$ ) in the noon sector ( $9 \leq \text{MLT} \leq 16$ ). The high occurrence rates of He<sup>+</sup> band waves are located in the predawn ( $3 \leq \text{MLT} \leq 6$ ) and morning ( $8 \leq \text{MLT} \leq 11$ ) sectors at relatively smaller L-shells ( $3 \leq L \leq 4.5$ ; Figure 3e). Compared with their H<sup>+</sup> and He<sup>+</sup> band counterparts, O<sup>+</sup> band EMIC waves are less frequently observed in the inner magnetosphere (Figure 3f). They mainly occur at small L-shells ( $3 \leq L \leq 4$ ) and have a little higher occurrence rate in the predawn ( $2 \leq \text{MLT} \leq 4$ ) sector. Figure 4 illustrates the distribution of three EMIC wave bands in the L-MLAT plane. These waves are mainly observed at lower magnetic latitudes with  $|\text{MLAT}| < 10^\circ$ , where it is also considered as the main source region of EMIC waves (Denton et al., 2014; Usanova et al., 2013). Interestingly, from H<sup>+</sup> band to He<sup>+</sup> band to O<sup>+</sup> band EMIC waves, there is a clear trend that their preferential region moves closer to the Earth.

We have further investigated the wave normal angle and polarization of EMIC waves, since they are key parameters for understanding the generation mechanism and wave-particle interactions. Figure 5 shows the distribution of wave normal angle  $\theta$  in the L-MLT and L-MLAT planes for H<sup>+</sup> band, He<sup>+</sup> band, and O<sup>+</sup> band waves, respectively. The  $\theta$  is given by the median value of wave normal angles for all time points in each bin. To reduce the statistical error, the bins containing less than 150 time points (i.e., 20 min of wave observations) have been discarded. The H<sup>+</sup> band waves typically have very small wave normal angles ( $< 30^\circ$ ), but their wave normal angles will become relatively larger at the larger magnetic latitude or L-shell (Figures 5a and 5d), which is consistent with the theoretical prediction (Andre, 1985). In Figures 5b and 5e, we find that He<sup>+</sup> band waves generally have moderate wave normal angles ( $30^\circ - 40^\circ$ ), and they also become more oblique at larger magnetic latitude or L-shell. However, O<sup>+</sup> band waves are observed to have either very small  $\theta$  ( $< 20^\circ$ ) or very large  $\theta$  ( $> 50^\circ$ ), and their wave normal angles seem to be independent on locations (Figures 5c and 5f).

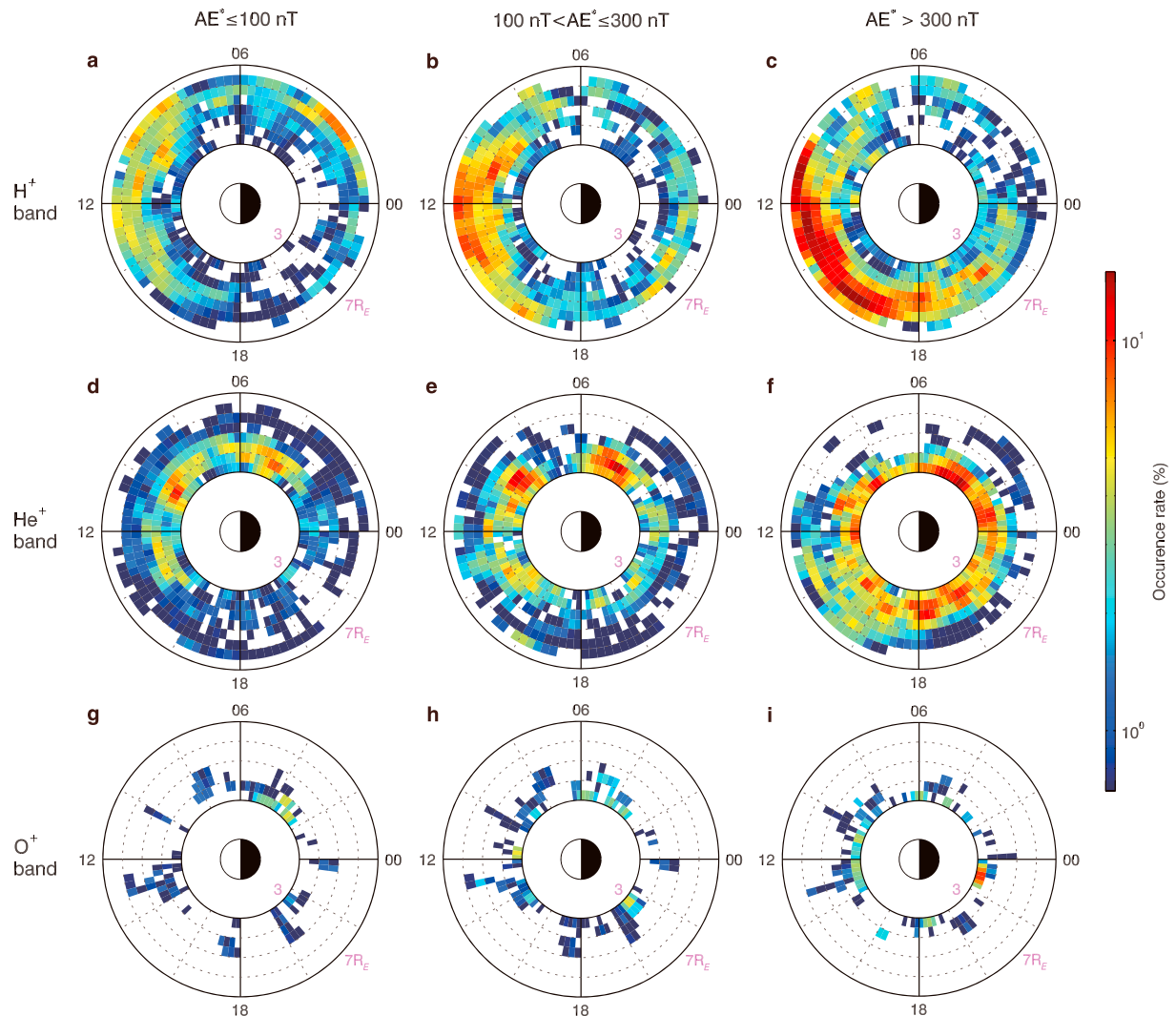


**Figure 7.** The distribution of occurrence rate of three band waves under three different geomagnetic conditions: (a, d, g)  $AE^* \leq 100$  nT, (b, e, h)  $100 \text{ nT} < AE^* \leq 300$  nT, and (c, f, i)  $AE^* > 300$  nT. Here, the  $AE^*$  index represents the mean value of AE index over the previous 1 hr. The three rows from top to bottom correspond to  $H^+$  band,  $He^+$  band, and  $O^+$  band waves, respectively.

With the same format as Figure 5, the distributions of the median ellipticity  $\varepsilon$  in the L-MLT and L-MLAT planes for three band waves are presented in Figure 6.  $H^+$  band waves are found to be weakly left-handed polarized with  $-0.1 < \varepsilon < 0$  (Figure 6a) and tend to become linearly polarized at higher magnetic latitudes (Figure 6d). Except some linearly polarized events in the inner regions ( $L < 3.5$ ),  $He^+$  band waves are mainly left-handed polarized with  $\varepsilon \leq -0.2$  (Figure 6b). There is also a trend that the ellipticity of  $He^+$  band waves gradually increases with the magnetic latitude (Figure 6e). Surprisingly, most of  $O^+$  band waves are found to be linearly polarized or even weakly right-handed polarized in Figures 6c and 6f.

The dependences of EMIC waves on the geomagnetic activity are also considered in our study. Figure 7 shows the distributions of occurrence rate for three band waves in three categories of  $AE^*$  index:  $AE^* < 100$  nT,  $100 \text{ nT} < AE^* \leq 300$  nT, and  $AE^* > 300$  nT. Here, the  $AE^*$  index for each data point is defined as the average value of AE index over the previous 1 hr (Li et al., 2009). In each category of  $AE^*$  index, the occurrence rate in each bin is given by the ratio between the total time of EMIC wave observation and the amount of dwell time that Van Allen Probes have in the same bin and  $AE^*$  category. During quiet times ( $AE^* \leq 100$  nT),  $H^+$  band waves are mainly observed on the dayside (Figure 7a). With the enhancement of geomagnetic activity, the occurrence rate of  $H^+$  band waves significantly increases in the noon

sector, and their preferential region even extends to the dusk sector (Figures 7b and 7c). Figures 7d–7f suggest that the main source regions (predawn and morning sectors) of  $\text{He}^+$  band waves do not show significant changes under different geomagnetic conditions, while during active geomagnetic periods, there is a clear enhancement of occurrence rate for  $\text{He}^+$  band waves, especially in the dusk and evening sectors. Under low and moderate geomagnetic conditions,  $\text{O}^+$  band waves preferentially occur at  $2 \leq \text{MLT} \leq 4$  below  $L = 4$  (Figures 7g–7h), which is consistent with the main source region shown in Figure 3f. However, most of  $\text{O}^+$  band waves are detected at the midnight ( $22 \leq \text{MLT} \leq 24$ ) sector at  $L < 3.5$  when the substorm injection is strong (Figure 7i).

Figure 8 illustrates the distribution of median normalized amplitude  $\delta B/B_0$  in the L-MLT plane under different levels of geomagnetic activities, where wave amplitude  $\delta B$  is the root-mean-square of integration over magnetic spectrum density in each frequency band. To make the statistics more convincing, we only retain the bins containing at least 150 data points (20 min) in Figure 8. The  $\text{H}^+$  band EMIC waves have significant magnetic amplitudes during quiet and moderate geomagnetic activities (Figures 8a and 8b) in their main source (noon sector). And their amplitudes become even larger in the dusk sector when  $\text{AE}^* > 300\text{nT}$  (Figure 8c). As shown in Figures 8d–8f, the magnetic amplitudes of  $\text{He}^+$  band waves on the dayside are comparable with or even stronger than those of  $\text{H}^+$  band waves. Moreover, they have much larger amplitudes in the dusk and evening sectors at  $4 \leq L \leq 6$  under active geomagnetic conditions. Clearly,  $\text{O}^+$  band waves have the smallest normalized amplitude among three band waves, and their amplitudes seem to be independent on the  $\text{AE}^*$  index.

#### 4. Conclusions and Discussions

We have restudied  $\text{H}^+$  band,  $\text{He}^+$  band, and  $\text{O}^+$  band EMIC waves with the magnetic data from Van Allen Probes twin satellites over a prolonged time period from 8 September 2012 to 31 December 2017 (totally 64 months) in the inner magnetosphere ( $3 \leq L \leq 7$ ). We have not only presented the global distribution, wave normal angle, and ellipticity of EMIC waves, but also investigated the dependence of their occurrence rates and magnetic amplitudes on the  $\text{AE}^*$  index. Our comprehensive statistical study is a valuable supplement to previous ones based on other probes. The principle results are summarized as below:

1.  $\text{H}^+$  band waves are preferentially detected at relatively larger L-shells ( $5 \leq L \leq 6.5$ ) in the noon sector ( $9 \leq \text{MLT} \leq 16$ ), whose main source region is near the magnetic equator with  $|\text{MLAT}| < 10^\circ$ .  $\text{H}^+$  band waves typically have very small wave normal angles ( $< 30^\circ$ ) and weakly left-hand polarization with  $-0.1 < \varepsilon < 0$ , but they become more oblique and linearly polarized at the larger magnetic latitudes or L-shells. With the increase of geomagnetic activity, their occurrence rate significantly increases in the noon sector, and their source region can extend to the dusk sector. Meanwhile,  $\text{H}^+$  band waves with significant magnetic amplitude occur around noon sector.
2.  $\text{He}^+$  band waves usually occur in the predawn ( $3 \leq \text{MLT} \leq 6$ ) and morning ( $8 \leq \text{MLT} \leq 11$ ) sectors at relatively smaller L-shells ( $3 \leq L \leq 4.5$ ). They are also mainly observed at lower magnetic latitudes with  $|\text{MLAT}| < 10^\circ$ .  $\text{He}^+$  band waves generally have moderate wave normal angles ( $30^\circ - 40^\circ$ ) and left-hand polarization ( $\varepsilon \leq -0.2$ ), and they also become more oblique and linearly polarized at the larger magnetic latitudes or L-shells. During active geomagnetic periods, there is a clear enhancement of occurrence rate for  $\text{He}^+$  band waves, especially in the dusk and evening sectors. Their magnetic amplitudes are comparable with or even stronger than those of  $\text{H}^+$  band waves on the dayside. Moreover, they have much larger amplitudes in the dusk and evening sectors under active geomagnetic conditions.
3.  $\text{O}^+$  band EMIC waves mainly occur at small L-shells ( $3 \leq L \leq 4$ ) and have a little higher occurrence rate in the pre-dawn ( $2 \leq \text{MLT} \leq 4$ ) sector.  $\text{O}^+$  band waves are observed to have either very small  $\theta$  ( $< 20^\circ$ ) or very large  $\theta$  ( $> 50^\circ$ ), and they are typically linearly or even weakly right-handed polarized. During active period, most of  $\text{O}^+$  band waves are detected at the midnight sector at  $L < 3.5$ .  $\text{O}^+$  band waves are weakest among three band waves, and their amplitudes seem to be independent on the  $\text{AE}^*$  index.

EMIC waves have been widely statistically studied in many previous works (Allen et al., 2015; Jun et al., 2019a, 2019b; Meredith et al., 2014; Min et al., 2012; Saikin et al., 2015). However, due to the limited spatial coverage for one satellite, we need to combine the statistical results based on various satellites to get a comprehensive and reliable EMIC wave model in the Earth's magnetosphere. Cluster satellites can measure EMIC waves at large magnetic latitudes due to their polar orbits (Meredith et al., 2014), while THEMIS



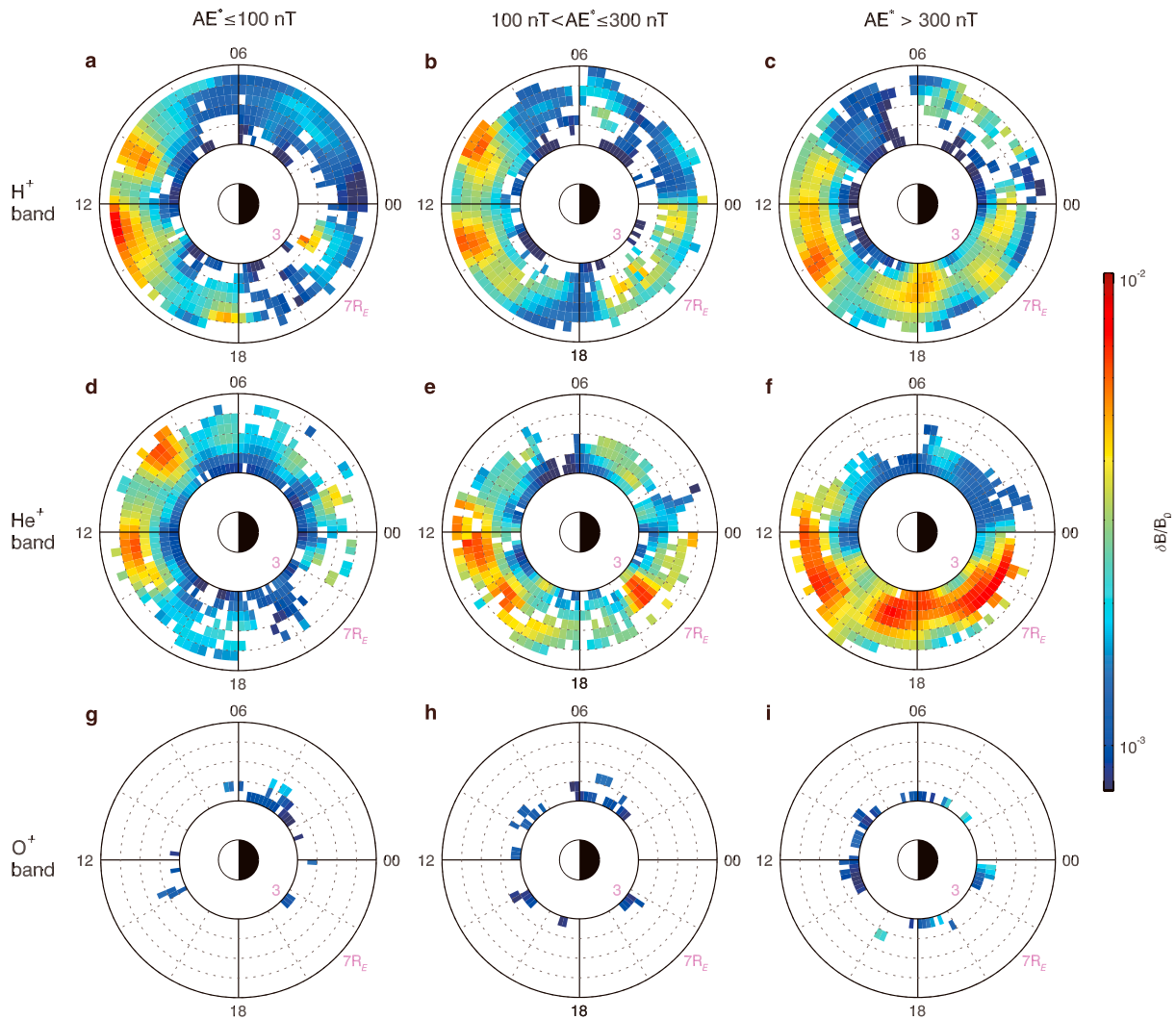


**Figure 8.** The distribution of normalized magnetic amplitude presented in the same format as that in Figure 7.

probes can provide a good coverage over MLT at the equatorial region but at relatively larger L-shells  $L > 7$  (Min et al., 2012). As a supplement, Van Allen Probes cover all MLT in the inner ( $L < 6.5$ ) magnetosphere near the magnetic equator. Using the first 22-month data, Saikin et al. (2015) have presented the distribution and wave properties for  $H^+$  band,  $He^+$  band, and  $O^+$  band waves. However, during this short time period, the number of detected wave events seems insufficient to give a reliable statistical result (Figures 3a–3c). Actually, we find that there are much more EMIC waves detected by Van Allen Probes after 2015 than before 2015. To obtain a more reliable wave model, we have analyzed Van Allen Probes data to study  $H^+$  band,  $He^+$  band, and  $O^+$  band EMIC waves over a prolonged time period (total 64 months). Our results can be considered as a valuable supplement to the existing studies about EMIC waves.

Another statistical study of EMIC waves with both Geostationary Operational Environmental Satellite system (GOES) and Van Allen Probes data has been performed in Jun et al. (2019a, 2019b), which categorized EMIC waves by particle injections. To identify whether EMIC wave events are associated with or without particle injections, they required that at least one GOES satellite must be located on the nightside. However, there are only 16-hr coverage of the nightside at 23–15 UT for GOES-13 and GOES-15, which means that EMIC wave events at 15–23 UT will be missed. Besides, their power threshold for identifying EMIC waves is also different from our study. These criteria result in the different spatial distributions of  $H^+$  band and  $He^+$  band waves from our results. They found  $H^+$  band waves are mostly observed outside

the plasmasphere at  $MLT = 12\text{--}15$  regardless of particle injections, while  $He^+$  band waves are preferentially detected inside the plasmasphere at  $MLT = 14\text{--}17$  with strong injections. However, the distributions of the wave normal angle and ellipticity for these two band waves are quite similar to this study.

The generation mechanism of EMIC waves is a long-standing problem in magnetosphere research. Both the linear theory (Chen et al., 2011; Horne & Thorne, 1993) and simulations (Hu et al., 2010) predict that EMIC waves are excited by anisotropic protons at the magnetic equator, which typically have very small wave normal angles and left-hand polarization. However, during their propagation toward polar regions, the waves tend to become more oblique and linearly polarized (Denton et al., 2014; Hu et al., 2010). The distributions of the wave normal angle and ellipticity of  $H^+$  band and  $He^+$  band waves in Figures 5 and 6 may provide some observational support. But for  $O^+$  band waves, they are mostly linearly polarized or weakly right-hand polarized. Moreover, some  $H^+$  band and  $He^+$  band waves are also observed with linear polarization near the magnetic equator, as shown in Figure 1. Many mechanisms have been proposed to explain the linearly polarized EMIC waves in their source region (Denton et al., 1992, 1996, 2014). However, there is still no direct evidence to support these theories (Yue et al., 2019). How to well explain those waves still requires a full study, which is beyond the scope of our paper. Besides, EMIC waves have been considered to play a key role in scattering relativistic electrons in the radiation belt (Carson et al., 2013; Gao et al., 2015; Ni et al., 2015; Zhang et al., 2016). Our study can provide a more precise EMIC wave model to calculate energy and pitch angle diffusion coefficients, which are used to further assess the effects of EMIC waves on the radiation belt dynamics.

#### Acknowledgments

This work was supported by the NSFC grant 41527804, 41774151, 41604128, and 41631071, Youth Innovation Promotion Association of Chinese Academy of Sciences (2016395), Young Elite Scientists Sponsorship Program by CAST (2018QNRC001), and Key Research Program of Frontier Sciences, CAS (QYZDJ-SSW-DQC010). We also acknowledge the entire Van Allen Probes instrument group and the data obtained from <https://spdf.sci.gsfc.nasa.gov/pub/data/rbsp/>.

#### References

- Allen, R. C., Zhang, J.-C., Kistler, L. M., Spence, H. E., Lin, R.-L., Klecker, B., et al. (2015). A statistical study of EMIC waves observed by Cluster: 1. Wave properties. *Journal of Geophysical Research: Space Physics*, 120, 5574–5592. <https://doi.org/10.1002/2015JA021333>
- Anderson, B. J., Erlandson, R. E., & Zanetti, L. J. (1992). A statistical study of Pc 1–2 magnetic pulsations in the equatorial magnetosphere: 1. Equatorial occurrence distributions. *Journal of Geophysical Research*, 7(A3), 3075–3088. <https://doi.org/10.1029/91JA02706C>
- Anderson, B. J., Fuselier, S. A., & Murr, D. (1991). Electromagnetic ion cyclotron waves observed in the plasma depletion layer. *Geophysical Research Letters*, 18(11), 1955–1958. <https://doi.org/10.1029/91GL02238>
- Anderson, B. J., & Hamilton, D. C. (1993). Electromagnetic ion cyclotron waves stimulated by modest magnetospheric compressions. *Journal of Geophysical Research*, 98(A7), 11,369–11,382. <https://doi.org/10.1029/93JA00605>
- Anderson, B. J., Takahashi, K., Erlandson, R. E., & Zanetti, L. J. (1990). Pc1 pulsations observed by AMPTE/CCE in the Earth's outer magnetosphere. *Geophysical Research Letters*, 17(11), 1853–1856. <https://doi.org/10.1029/GL017i011p01853>
- Andre, M. (1985). Dispersion surfaces. *Journal of Plasma Physics*, 33(1), 1–19. <https://doi.org/10.1017/S0022377800002270>
- Carson, B. R., Rodger, C. J., & Clilverd, M. A. (2013). POES satellite observations of EMIC-wave driven relativistic electron precipitation during 1998–2010. *Journal of Geophysical Research: Space Physics*, 118, 232–243. <https://doi.org/10.1029/2012JA017998>
- Chen, H. Y., Gao, X. L., Lu, Q. M., & Wang, S. (2018). In situ observations of harmonic Alfvén waves and associated heavy ion heating. *The Astrophysical Journal*, 859(2), 120. <https://doi.org/10.3847/1538-4357/aabee2>
- Chen, L., Thorne, R. M., & Bortnik, J. (2011). The controlling effect of ion temperature on EMIC wave excitation and scattering. *Geophysical Research Letters*, 38, L16109. <https://doi.org/10.1029/2011GL048653>
- Chen, L., Thorne, R. M., & Horne, R. B. (2009). Simulation of EMIC wave excitation in a model magnetosphere including structured high-density plumes. *Journal of Geophysical Research*, 114, A07221. <https://doi.org/10.1029/2009JA014204>
- Cornwall, J. M. (1965). Cyclotron instabilities and electromagnetic emissions in the ultra low frequency and very low frequency ranges. *Journal of Geophysical Research*, 70(1), 61–69. <https://doi.org/10.1029/JZ070i001p00061>
- Denton, R. E., Anderson, B. J., Ho, G., & Hamilton, D. C. (1996). Effects of wave superposition on the polarization of electromagnetic ion cyclotron waves. *Journal of Geophysical Research*, 101(A11), 24,869–24,885. <https://doi.org/10.1029/96JA02251>
- Denton, R. E., Hudson, M. K., & Roth, I. (1992). Loss-cone-driven ion cyclotron waves in the magnetosphere. *Journal of Geophysical Research*, 97(A8), 12,093–12,103. <https://doi.org/10.1029/92JA00954>
- Denton, R. E., Jordanova, V. K., & Fraser, B. J. (2014). Effect of spatial density variation and  $O^+$  concentration on the growth and evolution of electromagnetic ion cyclotron waves. *Journal of Geophysical Research: Space Physics*, 119, 8372–8395. <https://doi.org/10.1002/2014JA020384>
- Gao, X., Li, W., Bortnik, J., Thorne, R. M., Lu, Q., Ma, Q., et al. (2015). The effect of different solar wind parameters upon significant relativistic electron flux dropouts in the magnetosphere. *Journal of Geophysical Research: Space Physics*, 120, 4324–4337. <https://doi.org/10.1002/2015JA021182>
- Gao, X. L., Lu, Q. M., Li, X., Shan, L. C., & Wang, S. (2013). Electromagnetic proton/proton instability and its implications for ion heating in the extended fast solar wind. *The Astrophysical Journal*, 764(1), 71. <https://doi.org/10.1088/0004-637X/764/1/71>
- Gary, S. P., Liu, K., & Chen, L. (2012). Alfvén-cyclotron instability with singly ionized helium: Linear theory. *Journal of Geophysical Research*, 117, A08201. <https://doi.org/10.1029/2012JA017740>
- Horne, R. B., & Thorne, R. M. (1993). On the preferred source location for convective amplification of ion cyclotron waves. *Journal of Geophysical Research*, 98(A6), 9233–9247. <https://doi.org/10.1029/92JA02972>
- Hu, Y., Denton, R. E., & Johnson, J. R. (2010). Two-dimensional hybrid code simulation of electromagnetic ion cyclotron waves of multi-ion plasmas in a dipole magnetic field. *Journal of Geophysical Research*, 115, A09218. <https://doi.org/10.1029/2009JA015158>
- Jun, C.-W., Yue, C., Bortnik, J., Lyons, L. R., Nishimura, Y. T., & Kletzing, C. A. (2019a). EMIC wave properties associated with and without injections in the inner magnetosphere. *Journal of Geophysical Research: Space Physics*, 124, 2029–2045. <https://doi.org/10.1029/2018JA026279>

- Jun, C.-W., Yue, C., Bortnik, J., Lyons, L. R., Nishimura, Y. T., Kletzing, C. A., et al. (2019b). A statistical study of EMIC waves associated with and without energetic particle injection from the magnetotail. *Journal of Geophysical Research: Space Physics*, 124, 433–450. <https://doi.org/10.1029/2018JA025886>
- Kessel, R. L., Fox, N. J., & Weiss, M. (2012). The radiation belt storm probes (RBSP) and space weather. *Space Science Reviews*, 179(1-4), 531–543. <https://doi.org/10.1007/s11214-012-9953-6>
- Kletzing, C. A., Kurth, W. S., Acuna, M., MacDowall, R. J., Torbert, R. B., Averkamp, T., et al. (2013). The Electric and Magnetic Field Instrument Suite and Integrated Science (EMFISIS) on RBSP. *Space Science Reviews*, 179(1-4), 127–181. <https://doi.org/10.1007/s11214-013-9993-6>
- Li, W., Thorne, R. M., Angelopoulos, V., Bortnik, J., Cully, C. M., Ni, B., et al. (2009). Global distribution of whistler-mode chorus waves observed on the THEMIS spacecraft. *Geophysical Research Letters*, 36, L09104. <https://doi.org/10.1029/2009GL037595>
- Lu, Q. M., Guo, F., & Wang, S. (2006). Magnetic spectral signatures in the terrestrial plasma depletion layer: Hybrid simulations. *Journal of Geophysical Research*, 111, A04207. <https://doi.org/10.1029/2005JA011405>
- Lu, Q. M., & Wang, S. (2006). Electromagnetic waves downstream of quasi-perpendicular shocks. *Journal of Geophysical Research*, 111, A05204. <https://doi.org/10.1029/2005JA011319>
- Mauk, B. H., Fox, N. J., Kanekal, S. G., Kessel, R. L., Sibeck, D. G., & Ukhorskiy, A. (2013). Science objectives and rationale for the Radiation Belt Storm Probes mission. *Space Science Reviews*, 179(1-4), 3–27. <https://doi.org/10.1007/s11214-012-9908-y>
- Means, J. D. (1972). Use of the three-dimensional covariance matrix in analyzing the polarization properties of plane waves. *Journal of Geophysical Research*, 77(28), 5551–5559. <https://doi.org/10.1029/JA077i028p05551>
- Meredith, N. P., Horne, R. B., Kersten, T., Fraser, B. J., & Grew, R. S. (2014). Global morphology and spectral properties of EMIC waves derived from CRRES observations. *Journal of Geophysical Research: Space Physics*, 119, 5328–5342. <https://doi.org/10.1002/2014JA020064>
- Meredith, N. P., Thorne, R. M., Horne, R. B., Summers, D., Fraser, B. J., & Anderson, R. R. (2003). Statistical analysis of relativistic electron energies for cyclotron resonance with EMIC waves observed on CRRES. *Journal of Geophysical Research*, 108(A6), 1250. <https://doi.org/10.1029/2002JA009700>
- Min, K., Lee, J., Keika, K., & Li, W. (2012). Global distribution of EMIC waves derived from THEMIS observations. *Journal of Geophysical Research*, 117, A05219. <https://doi.org/10.1029/2012JA017515>
- Ni, B., Cao, X., Zou, Z., Zhou, C., Gu, X., Bortnik, J., et al. (2015). Resonant scattering of outer zone relativistic electrons by multiband EMIC waves and resultant electron loss time scales. *Journal of Geophysical Research: Space Physics*, 120, 7357–7373. <https://doi.org/10.1002/2015JA021466>
- Saikin, A. A., Zhang, J.-C., Allen, R. C., Smith, C. W., Kistler, L. M., Spence, H. E., et al. (2015). The occurrence and wave properties of  $H^+$ ,  $He^+$ , and  $O^+$ -band EMIC waves observed by the Van Allen Probes. *Journal of Geophysical Research: Space Physics*, 120, 7477–7492. <https://doi.org/10.1002/2015JA021358>
- Sakaguchi, K., Kasahara, Y., Shoji, M., Omura, Y., Miyoshi, Y., Nagatsuma, T., et al. (2013). Akebono observations of EMIC waves in the slot region of the radiation belts. *Geophysical Research Letters*, 40, 5587–5591. <https://doi.org/10.1002/2013GL058258>
- Spence, H. E., Reeves, G. D., Baker, D. N., Blake, J. B., Bolton, M., Bourdarie, S., et al. (2013). Science Goals and Overview of the Radiation Belt Storm Probes (RBSP) Energetic Particle, Composition, and Thermal Plasma (ECT) Suite on NASA's Van Allen Probes Mission. *Space Science Reviews*, 179(1-4), 311–336. <https://doi.org/10.1007/s11214-013-0007-5>
- Thorne, R. M., & Horne, R. B. (1994). Energy transfer between energetic ring current  $H^+$  and  $O^+$  by electromagnetic ion cyclotron waves. *Journal of Geophysical Research*, 99(A9), 17,275–17,282. <https://doi.org/10.1029/94JA01007>
- Tsyganenko, N. A., & Sitnov, M. I. (2005). Modeling the dynamics of the inner magnetosphere during strong geomagnetic storms. *Journal of Geophysical Research*, 110, A03208. <https://doi.org/10.1029/2004JA010798>
- Usanova, M. E., Darrouzet, F., Mann, I. R., & Bortnik, J. (2013). Statistical analysis of EMIC waves in plasmaspheric plumes from Cluster observations. *Journal of Geophysical Research: Space Physics*, 118, 4946–4951. <https://doi.org/10.1002/jgra.50464>
- Usanova, M. E., Mann, I. R., Rae, I. J., Kale, Z. C., Angelopoulos, V., Bonnell, J. W., et al. (2008). Multipoint observations of magnetospheric compression-related EMIC Pc1 waves by THEMIS and CARISMA. *Geophysical Research Letters*, 35, L17S25. <https://doi.org/10.1029/2008GL034458>
- Xiao, F. L., Chen, L. X., He, Y. H., Su, Z. P., & Zheng, H. N. (2011). Modeling for precipitation loss of ring current protons by electromagnetic ion cyclotron waves. *Journal of Atmospheric and Solar-Terrestrial Physics*, 73(1), 106–111. <https://doi.org/10.1016/j.jastp.2010.01.007>
- Young, D. T., Perraut, S., Roux, A., de Villedary, C., Gendrin, R., Korth, A., et al. (1981). Wave-particle interactions near  $\Omega_{He^+}$  Observed on GEOS 1 and 2, 1. Propagation of ion cyclotron waves in  $He^+$ -rich plasma. *Journal of Geophysical Research*, 86(A8), 6755–6772. <https://doi.org/10.1029/JA086iA08p06755>
- Yu, X., Yuan, Z., Huang, S., Yao, F., Wang, D., Funsten, H. O., & Wygant, J. R. (2018). Excitation of  $O^+$  band EMIC waves through  $H^+$  ring velocity distributions: Van Allen Probe observations. *Geophysical Research Letters*, 45, 1271–1276. <https://doi.org/10.1002/2018GL077109>
- Yuan, Z., Liu, K., Yu, X., Yao, F., Huang, S., Wang, D., & Ouyang, Z. (2018). Precipitation of radiation belt electrons by EMIC waves with conjugated observations of NOAA and Van Allen satellites. *Geophysical Research Letters*, 45, 12,694–12,702. <https://doi.org/10.1029/2018GL080481>
- Yue, C., Jun, C. W., Bortnik, J., An, X., Ma, Q., Reeves, G. D., et al. (2019). The relationship between EMIC wave properties and proton distributions based on Van Allen probes observations. *Geophysical Research Letters*, 46, 4070–4078. <https://doi.org/10.1029/2019GL082633>
- Zhang, J.-C., Kistler, L. M., Moukikis, C. G., Klecker, B., Sauvaud, J.-A., & Dumlop, M. W. (2011). A statistical study of EMIC wave-associated  $He^+$  energization in the outer magnetosphere: Cluster/CODIF observations. *Journal of Geophysical Research*, 116, A11201. <https://doi.org/10.1029/2011JA016690>
- Zhang, X.-J., Li, W., Ma, Q., Thorne, R. M., Angelopoulos, V., Bortnik, J., et al. (2016). Direct evidence for EMIC wave scattering of relativistic electrons in space. *Journal of Geophysical Research: Space Physics*, 121, 6620–6631. <https://doi.org/10.1002/2016JA022521>